Analysis of accuracy and ambiguities in spatial measurements of birefringence in uniaxial anisotropic media

Bouhy, Julie; Dekoninck, Augustin; Voué, Michel; Deparis, Olivier

Published in:
Applied Optics

DOI:
10.1364/ao.463657

Publication date:
2022

Document Version
Peer reviewed version

Analysis of accuracy and ambiguities in spatial measurements of birefringence in uniaxial anisotropic media

BOUHY JULIE,[1,*] AUGUSTIN DEKONINCK,[2] VOUÉ MICHEL,[3] AND DEPARIS OLIVIER[1]

[1]*Department of Physics, Namur Institute of Structured Matter, University of Namur, 61 Rue de Bruxelles, 5000 Namur, Belgium*
[2]*Department of Geology, Institute of Life-Earth-Environment, University of Namur,61 Rue de Bruxelles, 5000 Namur, Belgium*
[3]*Physics of Materials and Optics Units, Research Institute for Materials Science and Engineering, University of Mons, 20 Place du Parc, 7000 Mons, Belgium*
[*]*julie.bouhy@unamur.be*

Abstract: Accuracy and ambiguities in retardance and optical axis orientation spatial measurements are analyzed in details in the context of the birefringence imaging method introduced by Shribak and Oldenbourg [Appl. Opt. **42**,3009 (2003)]. An alternative formula was derived in order to determine the optical axis orientation more accurately, and without indetermination in the case of a quarter-wave plate sample. Following Shribak and Oldenbourg's experimental configuration using two variable retarders, a linear polarizer and five polarization probes, we examined the effect of the swing angle χ, which selected the ellipticity of each polarization state, on the accuracy of retardance (Δ) and axis orientation (ϕ) measurements. Using a quarter-wave plate, excellent agreement between measured and expected values was obtained for both the retardance and the axis orientation, as demonstrated by statistical analysis of Δ and ϕ spatial distributions. The intrinsic ambiguity in the determination of Δ and ϕ for superimposed layers of transparent anisotropic cello-tape is discussed in details and solutions are provided to remove this ambiguity. An example of application of the method on geological samples is also presented. We believe our analysis will guide researchers willing to exploit this long-standing method in their laboratories.

1. Introduction

Birefringence is the property exhibited by uniaxial optical media, which present two refractive index values according to the polarization of light [1]. This phenomenon was first observed in 1669 in the Iceland spar (calcite) by Rasmus Bartholin. Birefringence origin can be either molecular or structural (form birefringence), or induced by mechanical strains, electric field (Pockels and Kerr effect) or magnetic field (Faraday effect) [1]. The measurement of birefringence or retardance is particularly significant not only in optical industry (quality control), but also in various domains such as medicine [2, 3], pharmacology [4] and geology [5]. In the field of photoelasticity [6], birefringence measurements give access to the distribution of mechanical stress in e.g. glass or plastics, which is of great interest for industrial or architectural applications. In the case of liquid crystals, retardance of which is controlled by the application of an electric field, birefringence must be accurately determined in order to provide the product with specifications, i.e calibration curves [7]. Also, birefringence measurements give direct information about solid-state phase transition [8]. Linear birefringence can be measured by means of different techniques such as interferometry [9], compensation [10, 11], polarimetry [12, 13] or modulation [8, 14]. In 2003, Shribak and Oldenbourg introduced an original technique for birefringence imaging [15], which

they further developed [16] and extended to diattenuation measurement [17]. Basically, the 2D spatial distributions of both the retardance and the optical axis orientation are determined over the beam spot-size. These techniques were commercialised under the trademark Polscope [18]. Among the various versions of Polscope, we refer herein to the most precise version that uses two variable retarders, a linear polarizer and five polarization states to probe an anisotropic uniaxial transparent sample. As pointed by the authors, the method suffers from intrinsic ambiguities in determining retardance and axis orientation. Experimentally, it is worth recalling that the input polarization states is selected by the angle χ, which is called the swing angle [15]. The angle χ is a key parameter, since it tunes the ellipticity. In this article, we examined the influence of the χ parameter on measurement accuracy and found the latter could be improved by increasing χ value. We also investigated ambiguity issues and provided solutions to mitigate them. Hereafter, we first introduce the theoretical framework by recalling the basic principle of the method developed by Shribak and Oldenbourg and we derive an alternative formula for optical axis orientation measurements. In the next two sections, the experimental setup is presented as well as its calibration with commercial products. Then, on the basis of measurement results we obtained with various birefringent samples, we discuss ambiguity issues and propose solutions to mitigate them. Finally, we illustrate the usefulness of our method for the characterization of natural samples, in particular a composite quartz/tourmaline thin section.

2. Theoretical framework

Let us consider a general case, where a monochromatic polarized light beam propagates along the z axis into an anisotropic, uniaxial and inhomogeneous medium with varying orientations of its optical axis according to the lateral spatial position (Fig.1). We assume that the optical axis is everywhere parallel to both faces of the medium, i.e. it lies in the (x, y) plane. This hypothesis is fulfilled not only in polarizing optical components (retardation plates, etc.) but also in anisotropic films such as those resulting from the alignment of molecules or structures parallel to the surface. Therefore, in general, the medium exhibits a 2D spatial distribution of retardance $\Delta(x, y)$ and optical axis orientation $\phi(x, y)$.

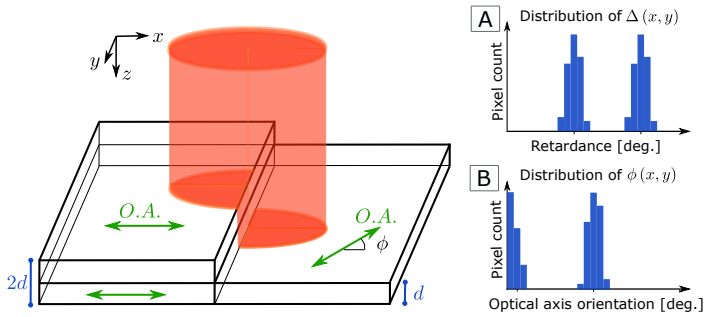

Fig. 1. Hypothetical samples, respectively composed of one layer (right) and two superimposed layers (left) of an anisotropic film of same retardance, have their optical axis oriented at different angles. (A) The retardance of the two superimposed layers is twice that of the single layer. (B) The optical axis orientations are 45° and 0°, respectively for one single layer and two superimposed layers. Blue bars around the mean values symbolize measurement inaccuracies or sample inhomogeneities.

Five input polarization states are successively generated by a tunable elliptical polarizer in order to probe the medium of interest and calculate both its retardance and optical axis orientation. The calculation is based on the five-frame algorithm of Shribak and Oldenbourg, derived from

the Jones matrix formalism [19]. It is noteworthy to remind that, in the Jones formalism, light is assumed to be entirely polarized.

The first input polarization state ψ_0 is circular whereas the four other ones (ψ_1, ψ_2, ψ_3 and ψ_4) are elliptical, with the same ellipticity ϵ but with azimuthal angles ϑ equal to 0°, 45°, 90° and 135°, respectively. The ellipticity ϵ of the input polarization states is controlled by the parameter χ, as $\chi = 90° - 2\epsilon$ [15]. Output polarization states, modified after propagation into the medium, are analyzed by a circular analyzer, the handedness of which is opposite to the handedness of the elliptical polarizer.

Any state of polarization can be decomposed in a basis of orthogonal polarization states e.g. horizontal and vertical ones or left-handed and right-handed ones. Since circular and elliptical polarization states were used, a circular polarization basis was chosen. Left-handed and right-handed polarization states are given by the following Jones vectors $\vec{E}_{\mathrm{L}} = \frac{1}{\sqrt{2}}\,[1, -i]^T$ and $\vec{E}_{\mathrm{R}} = \frac{1}{\sqrt{2}}\,[1, i]^T$, where T denotes transpose.

All polarization states can be expressed as a linear combination of these two polarization states, with a different phase shift between the components. For instance, horizontal linear polarization state is composed of in-phase left-handed and right-handed circular polarization states: $\vec{E}_{\mathrm{H}} = \vec{E}_{\mathrm{R}} + \vec{E}_{\mathrm{L}}$. Therefore, a right-handed circular analyzer will only select the right-handed component of the linear polarization state and the transmitted normalized intensity will be equal to 0.5. Left-handed polarization component will not be selected, so that the corresponding normalized intensity will be equal to zero whereas right-handed one will be entirely selected, giving a normalized intensity equal to one.

We can visualize states of polarization on the surface of the Poincaré sphere (Fig.2), where all states lie in the absence of depolarization. Polarization states located on the poles are circular and those lying on the equator are linear. All the other polarization states are elliptical. The Southern hemisphere contains left-handed states and the Northern hemisphere right-handed ones. On any latitude, the ellipticity is invariant and the azimuthal angle spans over a range from 0° to 360°. On any longitude, the azimuthal angle is fixed and the ellipticity spans from −45° to 45° (the tangent of ellipticity is given by the ratio of the ellipse axes).

Let us take the handedness of the five input polarization states to be left and the handedness of the circular analyzer to be right (or vice versa). By this choice, the polarization state ψ_0 is located on the Southern pole, which is opposite to the right circular analyzer location, leading to extinction configuration. The four other ones are located on the same latitude in the Southern hemisphere. The latitude is determined by the angle χ, which will be taken as a free parameter hereafter (Fig.2).

We now examine the influence of the χ parameter on the input polarization states and the normalized intensity transmitted through the analyzer, in the absence of any medium. As we work with a circular analyzer, only the ellipticity ϵ has an impact on the measured intensity, independently of the azimuthal angle ϑ. Since the circular polarization state ψ_0 has the opposite handedness to that of the circular analyzer, the intensity transmitted is equal to zero (i.e. extinction), as mentioned earlier. The ellipticity of the four elliptical polarization states, given by $\epsilon = 45° - \frac{\chi}{2}$, determines the latitude on the Poincaré sphere. When χ is increased, the polarization states ψ_1, ψ_2, ψ_3 and ψ_4 move away from the South pole. As a result, the transmitted intensity measured by a detector is increased, hence the signal to noise ratio is enhanced.

The effect of retardation plates is to transform the polarization states at the output. For instance, an half-wave plate (HWP) leads to a retardation of half a wavelength between ordinary and extraordinary light waves. The initial left circular polarization state $\psi_0^{(i)}$ at input is transformed in a final right circular polarization state $\psi_0^{(f)}$ at output, leading to full illumination of the detector, i.e. normalized intensity equal to one. The four elliptical polarization states remain on the same latitude, but are moved to the Northern hemisphere as the handedness is changed. As a result, the

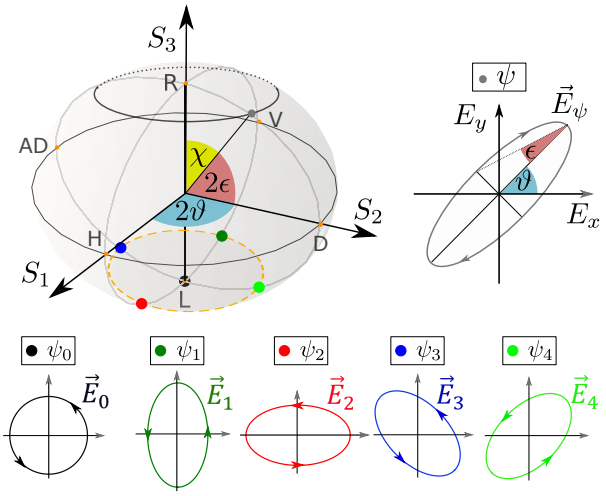

Fig. 2. All the polarization states on the surface of the Poincaré sphere are completely polarized. Those lying at the North and South poles are respectively right-handed circular (R) and left-handed circular (L), and those lying on the equator are linear. All the other polarization states are elliptical. Linear polarization states with azimuthal angle equal to 0°, 90°, 45° and 135° are horizontal (H), vertical (V), diagonal (D) and anti-diagonal (AD), respectively. The four elliptical polarization states ψ_1, ψ_2, ψ_3 and ψ_4 are located on the same latitude, which is determined by the χ parameter. The left-handed circular polarization state ψ_0 is located at the South pole. The ellipticity is defined by the angle ϵ and the ellipse inclination by the angle ϑ.

four intensities measured after the circular polarizer have to be the same. This particularity leads to an indetermination of the orientation of the optical axis of the half-wave plate (as it will be explained in section 3).

The intensity detected after the analyzer depends on the five input polarization states and the properties of the medium of interest, that is to say $\Delta(x, y)$ and $\phi(x, y)$. For the sake of simplicity, we consider a transparent medium, neglect depolarisation effects due to imperfect components (hardware dependent) and do not consider correction of background retardance obtained by removing the sample from the field of view [15]. These assumptions are equivalent, in eqs.7 of [15], to setting the distribution of the depolarized background illumination $I_{\min}(x, y) = 0$, the distribution of the illumination intensity on the sample $I_{\max}(x, y) = 1$ and the isotropic transparency $\tau(x, y) = 1$. The intensities $I_j(x, y, \Delta, \phi)$, with j referring to the corresponding input polarization state $\psi_j^{(i)}$, measured at each location (x, y) by an imaging detector, are expressed by:

$$
\begin{aligned}
I_0 &= I(\alpha = 90°, \beta = 180°) = \frac{1}{2}\left[1 - \cos\Delta\right], \\
I_1 &= I(\alpha = 90° - \chi, \beta = 180°) = \frac{1}{2}\left[1 - \cos\chi\cos\Delta + \sin\chi\sin(2\phi)\sin\Delta\right], \\
I_2 &= I(\alpha = 90° + \chi, \beta = 180°) = \frac{1}{2}\left[1 - \cos\chi\cos\Delta - \sin\chi\sin(2\phi)\sin\Delta\right], \\
I_3 &= I(\alpha = 90°, \beta = 180° - \chi) = \frac{1}{2}\left[1 - \cos\chi\cos\Delta - \sin\chi\cos(2\phi)\sin\Delta\right], \\
I_4 &= I(\alpha = 90°, \beta = 180° + \chi) = \frac{1}{2}\left[1 - \cos\chi\cos\Delta + \sin\chi\cos(2\phi)\sin\Delta\right],
\end{aligned} \tag{1}
$$

where $\Delta \in [0, 180°]$ and $\phi \in [0, 180°]$. Here, α and β denote, respectively, the retardances of two liquid crystals of the ellliptical polarizer (see next section), which define the input polarization state. Algebraic manipulation of these formula allows us to isolate Δ and ϕ, the two quantities of interest. In order to simplify the expressions of Δ and ϕ, two intermediate quantities are introduced (cf. eqs. 19 in [15]):

$$
\begin{aligned}
A \equiv \sin(2\phi)\tan\Delta &= \frac{I_1 - I_2}{I_1 + I_2 - 2I_0}\tan\frac{\chi}{2}, \\
B \equiv \cos(2\phi)\tan\Delta &= \frac{I_4 - I_3}{I_3 + I_4 - 2I_0}\tan\frac{\chi}{2},
\end{aligned} \tag{2}
$$

leading to the following expressions (cf. eqs. 20 in [15]):

$$
\Delta = \begin{cases} \arctan\left(\sqrt{A^2 + B^2}\right), \text{ if } I_1 + I_2 - 2I_0 \geq 0, \\ 180° - \arctan\left(\sqrt{A^2 + B^2}\right), \text{ if } I_1 + I_2 - 2I_0 < 0, \end{cases} \tag{3}
$$

$$
\phi = \frac{1}{2}\arctan\frac{A}{B}. \tag{4}
$$

If we examine eqs. 1 and 2, we see that both denominators of A and B are equal: $I_1 + I_2 - 2I_0 = I_3 + I_4 - 2I_0 = \cos\Delta\,(1 - \cos\chi)$. In order to determine the optical axis orientation, instead of using eq. 4, we propose to use an alternative formula in which the common denominator of A and B was simplified:

$$
\phi = \frac{1}{2}\arctan\left(\frac{I_1 - I_2}{I_4 - I_3}\right). \tag{5}
$$

The usefulness of this alternative expression will be highlighted later in this article. In the particular case of a quarter-wave plate (QWP), the common denominator of A and B is equal to zero. In this case, if we use eq. 4 to calculate the angle ϕ, the division by zero leads to an indetermination.

The parameter χ controls the ellipticity of input polarization states and, therefore, the intensity transmitted through the analyzer. We introduce here two additional parameters κ and η in order to analyze the influence of χ on the intermediate quantities A and B used to calculate the retardance and optical axis orientation. These parameters are defined by

$$
\kappa \triangleq \sqrt{(I_1 - I_2)^2 + (I_4 - I_3)^2} = \sin\chi\sin\Delta, \tag{6}
$$

$$
\eta \triangleq I_1 + I_2 - 2I_0 = \cos\Delta\,(1 - \cos\chi)\,. \tag{7}
$$

The parameter κ allows us to quantify the separation between the intensities I_j according to the retardance of the medium and the choice of the parameter χ. By dividing eq. 6 by eq.

7, we get $\tan\Delta = \frac{\kappa}{\eta}\frac{(1-\cos\chi)}{\sin\chi}$, which can be used as an alternative formula for determining the retardance. It is noteworthy that κ is equal to zero, both for a half-wave plate ($\Delta = 180°$) and an isotropic medium ($\Delta = 0°$) because the four output polarization states ($j = 1, 2, 3, 4$) lie on the same latitude on the Poincaré sphere. Therefore, all the four output intensities are equal, i.e. there is no separation between the intensities. In other words, when $\kappa = 0$, we face an ambiguity when distinguishing between an HWP or the absence of sample. The parameter κ monotonically rises with the increase of χ parameter when Δ spans from 0° to 90° whereas above $\Delta = 90°$, κ decreases monotonically until it reaches zero at $\Delta = 180°$ (Fig.3).

The parameter η defines the quadrant in which the retardance must lie according to eq. 3 ($]0°, 90°[$ or $]90°, 180°[$) and is also used to discriminate between ambiguous retardance values, i.e. $\Delta = 0°$ (isotropic medium) or $\Delta = 180°$ (half-wave plate). In the case of isotropic medium, $\eta = (1 - \cos\chi)$ whereas for the half-wave plate, $\eta = (\cos\chi - 1)$. For a small χ value, e.g. $\chi = 10°$, $\eta = \pm 0.015$ so that, in practice, it might be difficult to discriminate between an isotropic medium and an half-wave plate because of measurement noise. In such a situation, the choice of a higher χ value is recommended.

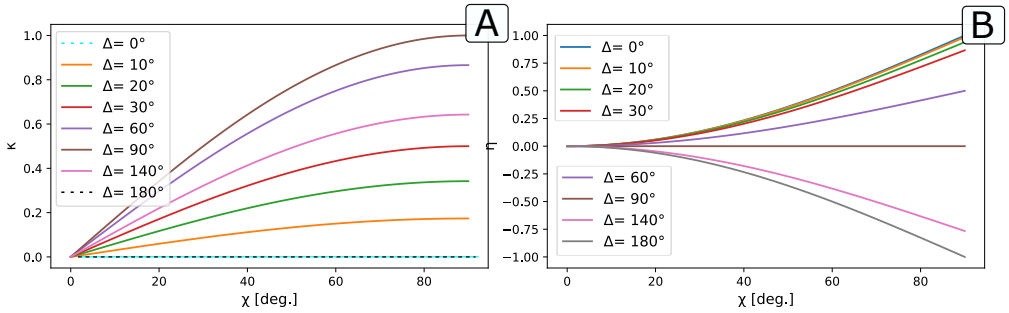

Fig. 3. A) The parameter κ, quantifying the separation between the measured intensities, is plotted as a function of parameter χ, for Δ between 0° and 180°. B) The parameter η, defining the quadrant in which Δ must lie, is plotted as a function of the parameter χ, for Δ between 0° and 180°.

3. Experimental setup

An experimental setup (Fig.4) was assembled from a HeNe laser (Thorlabs, Polarized HeNe Laser HNL150LB), an optical microscope (Olympus, BX53), light-polarising elements and a CCD camera (Olympus, SC50) in order to measure output light intensities corresponding to the five input polarization states and calculate the retardance and optical axis orientation distributions of the sample of interest.

Monochromatic light beam from the HeNe laser is collimated by two lenses and shaped by a pinhole. The collimated beam is elliptically polarized by a linear polarizer (Thorlabs, Glan-Taylor Polarizer) and two liquid crystal retardation plates LCA and LCB (Thorlabs, Uncompensated Half-Wave LC Retarder) with their optical axes respectively set at 0° and 45°. The retardance of both plates, noted respectively α and β, is controlled by applied voltage. The prepared polarization state is circular in the case of retardation values set to $\alpha = 90°$ and $\beta = 180°$. Otherwise, the ellipticity is induced by adding a positive or negative retardation χ to α and to β, but not on both simultaneously. The four elliptical polarization states produced have all the same ellipticity $\epsilon = 45° - \frac{\chi}{2}$, but different azimuthal angles equal to 0°, 45°, 90° and 135°.

The beam, emerging from the elliptical polarizer, is reflected by a mirror tilted at 45°. It is noteworthy that the mirror reflection modifies the polarization and flips its handedness, so that

it is necessary to choose the voltage applied to liquid crystals in a way to compensate for the polarization modifications induced by the mirror. The handedness of input polarization states is chosen to be the same as the handedness of circular analyzer, since the mirror flips it.

The reflected beam is focused on the sample by the condenser. The objective lens enables a 10× magnification of the sample. The polarized light emerging from the sample impinges on the circular analyzer. The circular analyzer is composed of a quarter-wave plate (Thorlabs, Multi-Order Quarter-Wave Plate) and a linear polarizer (Olympus, U-AN360P), the optical axes of which are respectively oriented at 45° and 0°. Adjustment of the quarter-wave plate angle is carefully realized with a polarimeter (Thorlabs, Polarimeter PAX1000VIS/M) placed on the top of the microscope. For this purpose, the LCs are removed from the optical path so that the beam is linearly polarized. Once the optical axis of the quarter-wave plate is properly oriented at 45°, the transmitted polarization state becomes circular and the position of the QWP is settled. The linear polarizer is then added in the optical path, and its proper orientation is selected thanks to the polarimeter.

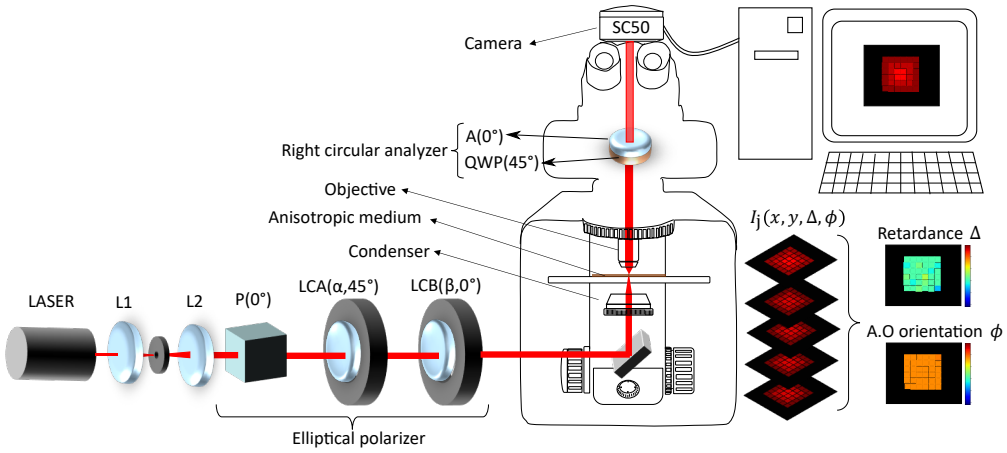

Fig. 4. Laser beam (632.8 nm) is collimated by two lenses (L_1, L_2) and elliptically polarized by a horizontal linear polarizer (P) and two liquid crystal retardation plates LCA and LCB, controlled by voltage. The optical axes of LCA and LCB are oriented at 45° and 0° respectively. The beam is reflected by a mirror oriented at 45°, focused by a condenser lens on the sample and transmitted throughout an objective lens (10×). The polarized beam is then directed towards the circular analyzer (A), composed of a quarter-wave plate and a linear polarizer (A) oriented so that the optical axis form an angle of 45°. The intensity of the beam at the output of the circular analyzer is measured by the CCD camera (SC50) of the microscope (BX53).

For each input polarization state $\psi_j^{(i)}$ where $j \in [0, 4]$, the intensity distribution $I_j\ (x, y; \Delta, \phi)$ detected by 16-bit camera (2560 × 1920 pixels) is recorded for further processing. All measurements are made with a ×10 objective lens and the image dimension is equal to 5632 μm × 4224 μm. The exposure time used to record the intensity distribution is extracted from image metadata for each configuration and used to calculate the intensity for an identical duration for all the configurations. This calculated intensity is directly used to determine the retardance and the orientation in each pixel of the image.

4. Calibration of measurement system

The calibration of the experimental setup consisted in determining the values of voltage to be applied to the liquid crystals in such a way to obtain the desired five input polarization states, with the ellipticity ϵ chosen beforehand. The calibration was carried out without sample and with two retardation plates as etalon: a quarter-wave plate (Thorlabs, WPQSM05-633) and half-wave plate (Thorlabs, WPHSM05-633). The quarter-wave plate allowed us to check the retardance and the orientation of the optical axis, whereas it was only possible to check the retardance of the half-wave plate, because of the indetermination on the orientation of the optical axis (see discussion below).

The retardation plate under test was placed at a particular angle and the control voltages applied to retardation liquid crystal plates were chosen to induce retardations equal to $[\alpha, \beta] \in \{(90°, 180°), (90° - \chi, 180°), (90° + \chi, 180°), (90°, 180° - \chi), (90°, 180° + \chi)\}$ (Fig.5).

Expected values for retardance of quarter-wave plate and half-wave plate are 90° and 180°, respectively. Without sample, it must be measured $\Delta = 0°$. In all cases, the recorded images must be ideally uniform.

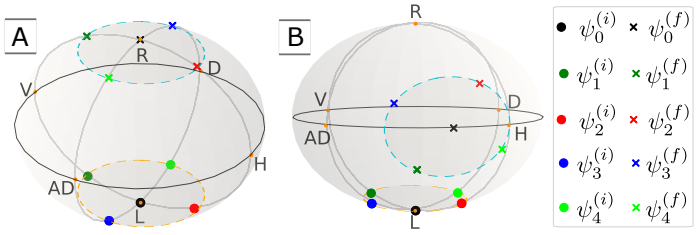

Fig. 5. The five input ($\psi_j^{(i)}$) and output ($\psi_j^{(f)}$) polarization states are depicted on the Poincaré sphere for A) HWP set at 0° B) QWP set at 120° (equivalent to −30°).

First order statistic analysis performed on Δ and ϕ values measured at $\chi = 60°$ for the quarter-wave plate oriented at an angle equal to $\phi = -30°$ gave mean values equal to $\langle\Delta\rangle = 89.77°$ and $\langle\phi\rangle = -30.17°$, and standard deviations equal to $\sigma_\phi = 1.60°$ and $\sigma_\Delta = 8.28°$. The Gaussian-fitted probability density function (pdf) with standard deviation σ and mean value μ, i.e. $f(x) = \frac{1}{\sigma\sqrt{2\pi}} \exp\left(\frac{1}{2}\left(\frac{x-\mu}{\sigma}\right)^2\right)$, is plotted in Fig.6 for Δ and ϕ measured on the QWP oriented at −30°. The excellent agreement between measured and expected values for both the retardance and the optical axis angle validates our measurement procedure.

In the absence of sample or with the HWP, measurements were performed only for the retardance since the optical axis orientation suffers from intrinsic ambiguity. Mean values measured at $\chi = 60°$ were equal to $\langle\Delta\rangle = 4.35°$ and $\langle\Delta\rangle = 174.24°$, respectively, and standard deviation values were equal to $\sigma_\Delta = 3.00°$ and $\sigma_\Delta = 3.54°$, respectively (Fig.6). In these cases, measured distributions departed from first-order statistics. As a result, peak values of the distributions did not match the mean values. The peak of the measured probability density was reached at $\Delta = 3°$ in the absence of sample, and at $\Delta = 176°$ with the HWP. The resolution limit of the experimental setup was therefore estimated to be around 4°, which corresponds to a noise level of $\Delta nd = \frac{\lambda}{2\pi}\frac{4\pi}{180} = 7.03$ nm.

5. Results and discussion

Hereafter, we first examine the effect of the swing angle χ on measurement accuracy and then the ambiguities in determining optical axis orientation.

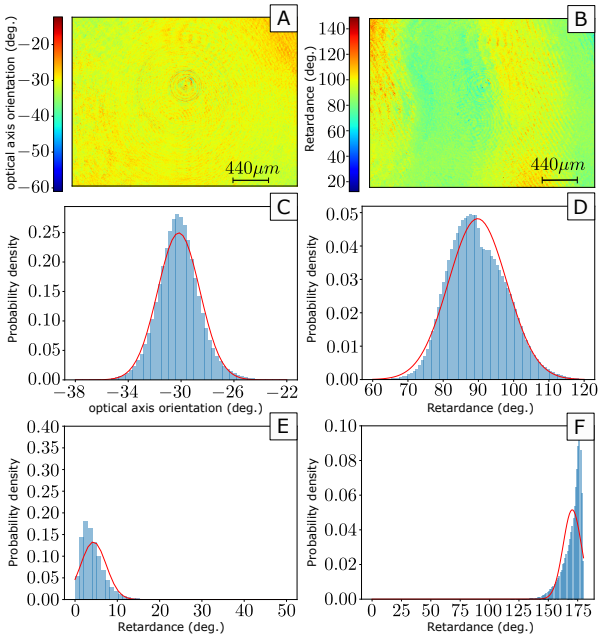

Fig. 6. Calibration with a QWP oriented at −30° (A-D), in the absence of sample (E) and with a HWP (F). The swing angle parameter of the measurement is $\chi = 60°$. A) Optical axis spatial distribution for the QWP. B) Retardance spatial distribution for the QWP. C) Probability density of optical axis distribution for the QWP. D) Probability density of retardance distribution for the QWP. E) Probability density of retardance distribution in the absence of sample. F) Probability density of retardance distribution with an HWP oriented at 0°.

5.1. Effect of χ parameter on measurement accuracy

In order to highlight the effect of the parameter χ on the measurement accuracy, a retardation plate (Olympus, U-TP137) was chosen to measure both Δ and ϕ according to χ, with χ varying in the range $[0°, 80°]$. The mean and standard deviation obtained from first order statistics performed on Δ and χ measured distributions (Table A1 (A)) are compared for different χ values (Fig.7).

On overall, increasing the value of χ leads to higher accuracy in the determination of the retardance and the optical axis orientation. Increase of χ has much more pronounced effect on the accuracy of retardance measurement, especially in the range $\chi \in [10°, 40°]$ (Fig.7 (A)). The parameter χ intervenes directly in the retardance formula (eq. 2), whereas it is not present in the optical axis orientation formula (eq. 5). In theory, χ should therefore not have any impact on calculation of ϕ. However, a small effect on optical axis orientation measurement accuracy (Fig.7 (B)) is observed for $\chi \in [10°, 40°]$. This is due to the increase of measured intensities separation with increasing χ, as discussed in section 2.

As expected, in the absence of sample, the measured retardance is close to $\Delta = 0°$ (Fig.8 (A,B)), since the ellipticity of the output polarization states ψ_1, ψ_2, ψ_3 and ψ_4 are all the same and $\eta \geq 0$. The accuracy saturates with the increase of χ values (Table A1 (B)). In the case of the HWP (Table A1 (C)), the increase of χ removes the ambiguity between $\Delta = 0°$ and $\Delta = 180°$, as discussed in section 2 (Fig.8 (C,D)).

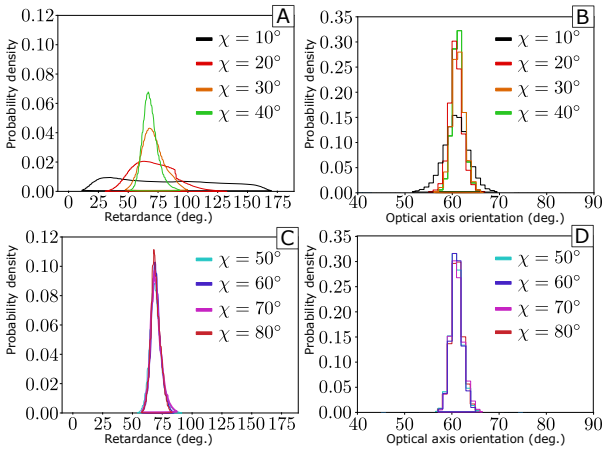

Fig. 7. Probability density drawn from pixel values of retardance (A,C) and optical axis orientation (B,D) for χ equal to 10°, 20°, 30° and 40° (top charts) and χ equal to 50°, 60°, 70° and 80° (bottom charts).

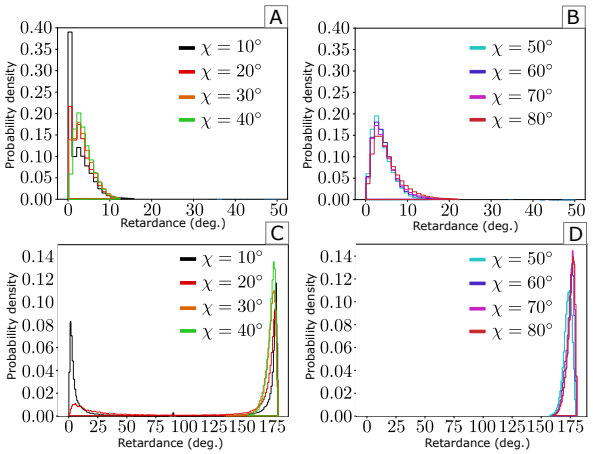

Fig. 8. Probability density drawn from pixel values of retardance in absence of sample ($\Delta = 0°$) for χ equal to 10°, 20°, 30° and 40° (A) and χ equal to 50°, 60°, 70° and 80° (B). Probability density drawn from pixel values of retardance of a HWP for χ equal to 10°, 20°, 30° and 40° (C) and χ equal to 50°, 60°, 70° and 80° (D).

5.2. Ambiguity on optical axis orientation

If the angle ϕ is calculated from eq. 4, we already noted that the optical axis orientation suffers from indetermination in the case of a quater-wave-plate (Thorlabs, WPMQ10M-633). This situation is illustrated in Fig.9 (A,C) for a quarter-wave plate oriented at $-30°$. However, thanks to our alternative expression of ϕ, i.e. (eq. 5), the indetermination on ϕ disappears (Fig.9 and Table A1 (D)). Both the map and the probability density obtained from eq. 4 show random ϕ values due to the indetermination. Those obtained from eq. 5 give almost uniform map with a narrow statistical distribution around the expected value.

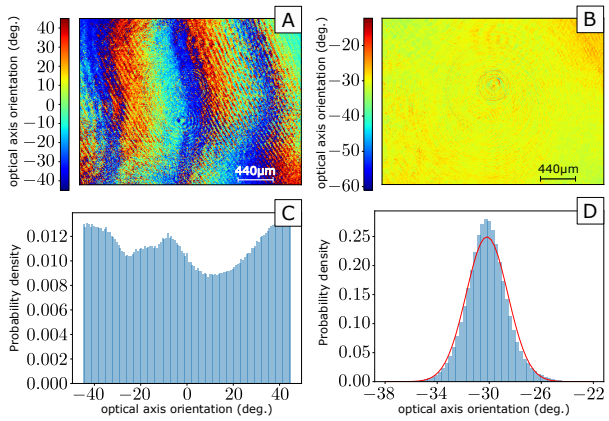

Fig. 9. Maps of the angle ϕ for a QWP oriented at $\phi = -30°$ calculated using eq. 4 (A) or eq. 5 (B). Probability density (C, D) drawn from pixel values in images (A, B), respectively.

Let us examine how is the indetermination removed thanks to our procedure. For an a priori unknown sample, the signs of the numerators of A and B allow us to determine the quadrant in which lies the angle that is solution of $\tan 2\phi = \left(\frac{I_1 - I_2}{I_4 - I_3}\right)$, with the angle 2ϕ being counted positive in anticlockwise direction from the horizontal axis. Two solutions exist, i.e. 2ϕ and $180° + 2\phi$, the latter being located in the opposite quadrant with respect to the former. The numerators of A and B are given by, see eqs. 1:

$$\begin{aligned} I_1 - I_2 &= \sin(\chi)\sin(2\phi)\sin(\Delta), \\ I_4 - I_3 &= \sin(\chi)\cos(2\phi)\sin(\Delta). \end{aligned} \tag{8}$$

From now, we assume that Δ and χ both span from $0°$ to $180°$, so that both $\sin\Delta$ and $\sin\chi$ are always positive. Therefore, the signs of the numerators of A and B are given by the signs of $\sin(2\phi)$ and $\cos(2\phi)$, respectively. A positive value of the product $(I_1 - I_2)(I_4 - I_3)$ indicates that the angle 2ϕ belongs either to the first or the third quadrant. Conversely, a negative value indicates that it belongs to either the second or the fourth quadrant.

We are interested to determine the angle ϕ, i.e. the optical axis orientation. Therefore, it is necessary to examine the signs of $I_1 - I_2$ and $I_4 - I_3$ independently in order to locate the angle in one of the four upper octants (Fig.10). Multiplication of the signs can lead to a flip between the fast and slow axis of the sample, e.g. the sign of $(I_1 - I_2)(I_4 - I_3)$ is positive for ϕ lying in the first and third octants, and negative in the second and fourth octants. For instance, without taking into account the signs of $I_1 - I_2$ and $I_4 - I_3$, an optical axis which forms an angle equal to $\phi = 100°$ can be identified either as $10°$ (white octants in Fig.10) or $100°$ (light gray octants). Indeed, $2\phi = 200°$ or $2\phi + 180° = 20°$ give the same value of the tangent. Now, taking into

account both the signs individually leads to angles equal either to $\phi = -80°$ or $100°$, which obviously define the same orientation (light gray octants).

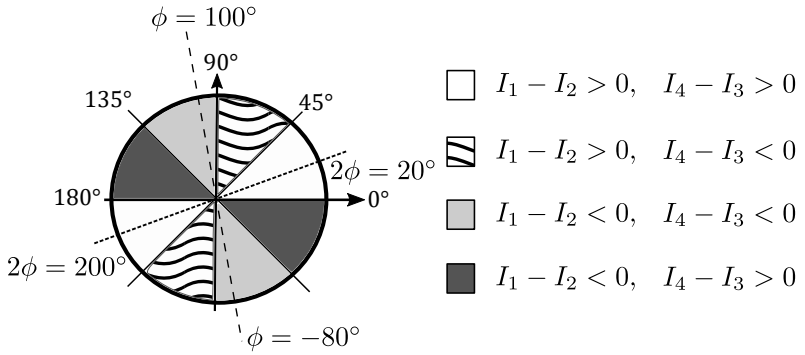

Fig. 10. Optical axis orientation is defined either by the angle ϕ or the angle $180° + \phi$ (octants of the same color). The signs of both the numerators of A and B are examined in order to determine the correct optical axis orientation. An example is shown for $\phi = 100°$.

In summary, the optical axis orientation can be determined without ambiguity when the signs of $I_1 - I_2$ and $I_4 - I_3$ are examined separately, as far as the retardance lies in the $[0°, 180°]$ range.

5.3. Ambiguity on retardance

In principle, the signs of both $\sin\Delta$ and $\cos\Delta$ allow us to determine the quadrant in which Δ lies. For instance, Δ lies in the first quadrant when $\sin\Delta > 0$ and $\cos\Delta > 0$. In practice, however, we have only access to measurements of the intensities from which we deduce Δ and ϕ. A retardance higher than $\Delta = 180°$ induce a flip of both the signs of $I_1 - I_2$ and $I_4 - I_3$ (eq. 8) which introduces an ambiguity in determination of ϕ if the range of Δ is not known a priori. This is why we had assumed $\Delta < 180°$ in our previous discussion about optical axis orientation.

We illustrate hereafter the ambiguity in retardance determination by a simple experiment realized using commercial transparent cello-tape as sample. The tape consisted of an anisotropic polymer film with a smooth surface. We first observed cello-tape layers with a polarizing optical microscope and concluded that this material was birefringent [20], [21] (Fig.11 (A,B)). With its thickness of about 50 μm, cello-tape is therefore a convenient sample for testing retardance measurement ambiguity. We then measured the retardance of one layer of cello-tape deposited on a glass plate and obtained $\Delta_{\text{cello},1} = 120°$ (Fig.11 (C,D)). We can predict that superimposing n layers should induce a retardance equal to $\Delta_{\text{cello},n} = n\Delta_{\text{cello},1}$. Hence, two and three layers should give $\Delta = 240°$ and $\Delta = 360°$, respectively.

However, measurements of the retardance for two and three layers led to $\Delta = 120°$ and $\Delta = 0°$, respectively (Fig.11 B.). In the former case, the parameter η (determined from measured intensities, eq. 7) was found to be negative so that, according to eq. 3, $\Delta = 180° - \arctan\sqrt{A^2 + B^2} = 180° - 60° = 120°$ and not $240°$ as expected.

Noting that $\tan\Delta = \sqrt{A^2 + B^2}$ is always positive, irrespective of the position of Δ in the quadrants, the formula of Δ must be adapted according to: $\Delta = 180° + \arctan\sqrt{A^2 + B^2}$ when Δ lies in the third quadrant and $\Delta = 360° - \arctan\sqrt{A^2 + B^2}$ when Δ lies in the fourth quadrant (Fig.12). In the first and second quadrants, the formula are the ones given by eq. 7. When $\Delta > 180°$, the sign of $\cos\Delta$ allows us to discriminate whether the retardance lies in the third or the fourth quadrant. The sign can be extracted from the measured intensities if we figure out that,

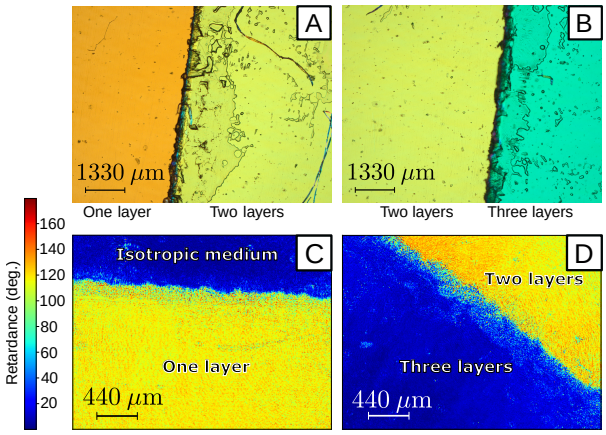

Fig. 11. (A,B) Polarizing optical microscope images of layers of cello-tape observed between crossed polarizers . A) One and two layers B) Two and three layers. Observation of colors indicates the birefringent nature of the sample. C) Map of the retardance of one cello-tape layer deposited on glass plate (isotropic medium). D) Map of the retardance imaging of two and three layers superimposed.

see eqs. 8

$$\cos\chi\cos\Delta = 1 - \frac{I_1 + I_2 + I_3 + I_4}{2}, \tag{9}$$

where χ is assumed to be in the range $]0°, 90°[$.

For two layers of cello-tape, we have $\cos\chi\cos\Delta < 0$. The retardance lies in the third quadrant and is given by $\Delta = 180° + \arctan\left(\sqrt{A^2 + B^2}\right)$, so $\Delta = 180° + 60° = 240°$ as expected. In the case of the three layers, we have $\cos\chi\cos\Delta > 0$ and $\Delta = 360° - 0° = 360°$, again as expected.

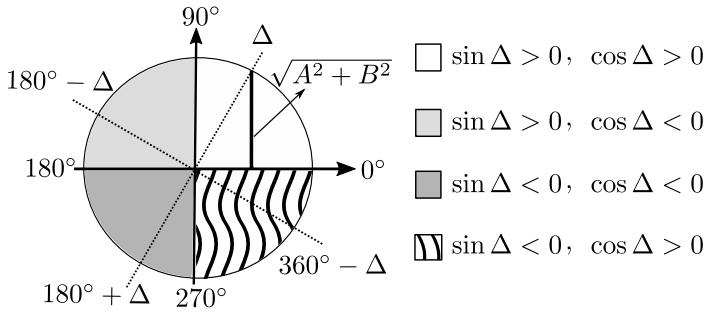

Fig. 12. Retardance, when calculated by $\Delta = \arctan\sqrt{A^2 + B^2}$, is always located in first quadrant. The formula used for calculates Δ must be adapted in the other cases: $180° - \Delta$, $180° + \Delta$ and $360° - \Delta$ in the second, third and fourth quadrants.

In summary, the measurements of Δ and ϕ are unavoidably ambiguous for an a priori unknown sample because the optical axis orientation angle ϕ and retardance Δ appear together in the expressions of A and B in eqs. 2, i.e. the unknowns are coupled in the equations. The ambiguity can be removed, however, if we know a priori that Δ lies in the range $[0°, 180°]$ or in the range $[180°, 360°]$.

5.4. Application to geological samples

In order to illustrate the usefulness of our method in the context of natural samples, we analyzed several geological thin sections with a thickness equal to 30 μm. The sample we selected for illustration is composed of a mixture of quartz (SiO2) and tourmaline $\left[(\mathrm{Ca, Na, K, Pb})(\mathrm{Al, Fe^{2+}, Fe^{3+}, Li, Mg, Mn^{2+}, Ti})_3(\mathrm{Al, Cr, Fe^{3+}, V})_6(\mathrm{Si_6O_{18}})(\mathrm{BO_3})_3(\mathrm{O, OH})_3\ (\mathrm{F, O, OH})\right]$ crystals. Both silicate minerals belong to the trigonal crystal system and are uniaxial. However, the signs of birefringence are different: quartz is positive and tourmaline is negative. Quartz is translucent and uncoloured under polarized light with a weak birefringence of $\Delta n \approx 0.009$, which enables recognition of quartz regions under optical microscope (Fig.13 A). Tourmaline is translucent with colours varying within a single crystal depending on its chemistry under polarized light (Fig.13 B). Its birefringence is stronger than quartz $\Delta n \in [0.015, 0.028]$. Under optical microscope, it is easy to recognize tourmaline regions, as they appear colored (Fig. 13 A)

Due to the natural origin of the sample, it is not guaranteed that the optical axis lies in the plane parallel to the sample surface, as assumed in the theoretical model (Fig.1). Moreover, quartz regions are actually composed of grains whose axis orientations differ, as it can be observed under polarized microscope (Fig.13 B). All these characteristics of composite natural samples are retrieved by our measurements: namely, distinct retardance peaks corresponding to different grains (Fig.13 (C,E)), with different optical axis orientations (Fig.13 (D,F)).

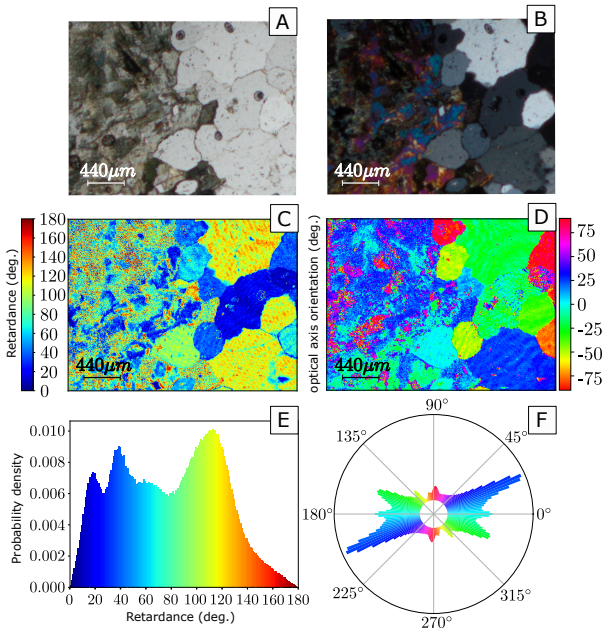

Fig. 13. Image of a 30 μm thin section of a mixture of quartz and tourmaline observed (A) with an optical microscope. (B) with a polarizing optical microscope, between crossed polarizers. (C) Map of the retardance. (D) Map of the optical axis orientation. Probability density (E) drawn from pixel values in image (C). Optical axis orientation (F) drawn on circular histogram from pixel values in image (D).

6. Conclusion

The accuracy and ambiguities in birefringence measurements were examined in details and our laboratory implementation was validated using reference samples. We proposed an alternative

formula for the calculation of the optical axis orientation, which improved the measurement accuracy and avoided the indetermination in the case of a QWP. The effect of the swing value χ on measurement accuracy was demonstrated and explained. We noted a clear improvement of the accuracy, especially on retardance, with monotonically increase of χ parameter in the range $[0°, 90°]$.

We examined the ambiguities in retardance determination thanks to a simple experiment based on commercial cello-tape, which is a common example of anisotropic transparent film. Different layers of cello-tape were superimposed, and the correct retardance value was identified according to Δ was higher or lower than $\Delta = 180°$.

We also applied our method for characterizing geological thin samples and showed it can help, e.g. determining the orientation of grains in a composite sample.

In the future, we intend to apply this measurement procedure to the characterisation of parchments, in the context of cultural heritage. Indeed, parchment, a non-opaque thin material processed from animal skin, is known to exhibit birefringence and determination of spatial distributions of local retardance and optical axis could bring valuable information on its state of conservation [22].

A. Appendix

The mean and standard deviation values of the measured probability density of Δ and ϕ are displayed in the following tables, for three different retardation plates (UTP-137, QWP and HWP) and without sample.

Table A1. (A) Mean and standard deviation values of the measured probability density of the retardance and optical axis orientation for a retardation plate UTP-137 oriented at 60°. The angles calculated with the original and alternative formula are respectively noted ϕ and ϕ_{new}. (B) Mean and standard deviation values of the measured probability density of retardance ($\langle\Delta\rangle$, σ_Δ) and of the fitted (Gaussian) probability density function (μ, σ) in absence of sample. The angle ϕ is not calculated as it is undetermined in the absence of sample. (C) Mean and standard deviation values of the measured probability density of the retardance for an HWP. The angle is not calculated as it is undetermined in the case of a HWP. (D) Mean and standard deviation values of the measured probability density of the retardance and optical axis orientation for a QWP oriented at −30°.

(A) UTP-137 oriented at 60°								
χ[°]	10	20	30	40	50	60	70	80
$\langle\Delta\rangle$ [°]	82.66	72.00	71.01	68.78	69.54	69.34	69.72	69.42
σ_Δ[°]	42.21	18.69	10.39	6.96	5.32	4.46	4.90	4.06
$\langle\phi\rangle_{\text{new}}$ [°]	60.77	60.83	61.17	61.24	61.00	61.01	61.12	61.12
$\sigma_{\phi,\text{new}}$[°]	3.43	1.55	1.50	1.30	1.30	1.27	1.38	1.31
$\langle\phi\rangle$ [°]	−17.78	−17.80	−25.87	−28.35	−28.42	−28.39	−28.58	−28.56
σ_ϕ[°]	25.59	22.68	13.33	6.74	4.47	2.58	1.40	2.07
(B) Absence of sample								
χ[°]	10	20	30	40	50	60	70	80
$\langle\Delta\rangle$ [°]	15.75	5.98	4.47	3.90	4.03	4.35	4.68	5.42
σ_Δ[°]	39.36	17.72	7.12	2.88	2.80	3.00	3.40	3.87
μ[°]	9.85	4.97	4.07	3.90	4.03	4.35	4.68	5.42
σ[°]	32.61	16.31	6.91	2.88	2.80	3.00	3.40	3.87
(C) HWP								
χ[°]	10	20	30	40	50	60	70	80
$\langle\Delta\rangle$ [°]	99.29	134.60	172.33	174.05	172.80	174.24	174.55	174.51
σ_Δ[°]	82.47	64.27	8.90	4.22	3.82	3.54	3.41	3.45
(D) QWP oriented at −30°								
χ[°]	10	20	30	40	50	60		
$\langle\Delta\rangle$[°]	90.23	87.70	87.94	89.48	89.23	89.77		
σ_Δ[°]	46.23	20.63	12.63	9.90	8.79	8.28		
$\langle\phi_{\text{new}}\rangle$[°]	−30.09	−30.31	−30.27	−30.18	−30.25	−30.17		
$\sigma_{\phi,\text{new}}$[°]	4.65	2.22	1.76	1.66	1.65	1.60		

Disclosures

The authors declare no conflicts of interest.

References

1. M. C. T. Bahaa E. A. Saleh, *Polarization and Crystal Optics* (John Wiley and Sons, Ltd, 1991), chap. 6, pp. 193–237.
2. M. C. Pierce, J. Strasswimmer, H. Park, B. Cense, and J. F. de Boer, "Birefringence measurements in human skin using polarization-sensitive optical coherence tomography," J. Biomed. Opt. **9**, 287 – 291 (2004).
3. B. Cense, T. C. Chen, B. H. Park, M. C. Pierce, and J. F. de Boer, "In vivo depth-resolved birefringence measurements of the human retinal nerve fiber layer by polarization-sensitive optical coherence tomography," Opt. Lett. **27**, 1610–1612 (2002).
4. C. F. Chignell and D. K. Starkweather, "Optical studies of drug-protein complexes," Mol. Pharmacol. **7**, 229–237 (1971).
5. A. M. Hofmeister, R. B. Schaal, K. R. Campbell, S. L. Berry, and T. J. Fagan, "Prevalence and origin of birefringence in 48 garnets from the pyrope-almandine-grossularite-spessartine quaternary," Am. Mineral. **83**, 1293–1301 (1998).
6. H. Mueller, "The therory of photoelasticity," J. Am. Ceram. Soc. **21**, 27–33 (1938).
7. S.-T. Wu, U. Efron, and L. D. Hess, "Birefringence measurements of liquid crystals," Appl. Opt. **23**, 3911–3915 (1984).
8. I. G. Wood and A. M. Glazer, "Ferroelastic phase transition in bivo4 i. birefringence measurements using the rotating-analyser method," J. Appl. Crystallogr. **13**, 217–223 (1980).
9. R. C. Miller and A. Savage, "Temperature dependence of the optical properties od ferroelectric $LiNbO_3$ and $LiTaO_3$," Appl. Phys. Lett. **9**, 169–171 (1966).
10. R. Evans, "Crystals and the polarising microscope by nh hartshorne and a. stuart," Acta Crystallogr. **13**, 853–853 (1960).
11. J. C. Tolédano, "Phenomenological model for the structural transition in benzil," Phys. Rev. B **20**, 1147–1156 (1979).
12. R. T. Harley and R. M. Macfarlane, "A determination of the critical exponent beta in TbVO4and DyVO4using linear birefringence," J. Phys. C: Solid State Phys. **8**, L451–L455 (1975).
13. W. T. Welford, "Principles of optics (5th Edition). M. Born, E. Wolf Pergamon Press, Oxford, 1975, pp xxviii + 808, £9.50," Opt. Laser Technol. **7**, 696 (1975).
14. D. J. Benard and W. C. Walker, "Modulated polarization measurement of structural phase transitions in kmnf3," Rev. Sci. Instruments **47**, 122–127 (1976).
15. M. Shribak and R. Oldenbourg, "Techniques for fast and sensitive measurements of two-dimensional birefringence distributions," Appl. Opt. **42**, 3009–3017 (2003).
16. M. Shribak, "Complete polarization state generator with one variable retarder and its application for fast and sensitive measuring of two-dimensional birefringence distribution," J. Opt. Soc. Am. A **28**, 410–419 (2011).
17. S. B. Mehta, M. Shribak, and R. Oldenbourg, "Polarized light imaging of birefringence and diattenuation at high resolution and high sensitivity," J. Opt. **15**, 094007 (2013).
18. "OpenPolScope," https://openpolscope.org/. Accessed: 2022-02-30.
19. R. C. Jones, "A new calculus for the treatment of optical systemsv. a more general formulation, and description of another calculus," J. Opt. Soc. Am. **37**, 107–110 (1947).
20. A. Beléndez, E. Fernández, J. Francés, and C. Neipp, "Birefringence of cellotape: Jones representation and experimental analysis," Eur. J. Phys. **31**, 551–561 (2010).
21. M. A. Blanco, M. Yuste, and C. Carreras, "Undergraduate experiment designed to show the proportionality between the phase difference and the thickness of a uniaxial crystal," Am. J. Phys. **65**, 784–787 (1997).
22. V. Vilde, M. Fourneau, C. Charles, D. V. Vlaender, J. Bouhy, Y. Poumay, and O. Deparis, "Use of polarised light microscopy to improve conservation of parchment," Stud. Conserv. **64**, 284–297 (2019).